Nuclear Science and Techniques (2025) 36:2
https://doi.org/10.1007/s41365-024-01544-9

A single-pixel elemental imaging method using neutron-induced gamma-ray activation

Can Cheng[1,2] · Yong-Ji Xie[3] · Xun-Rong Xia[1] · Jia-Yu Gu[1] · Dong Zhao[2] · Yi-Ze Chen[2] · Ai-Yun Sun[2] · Xu-Wen Liang[2] · Wen-Bao Jia[2] · Da-Qian Hei[2,4]

Received: 13 September 2023 / Revised: 30 January 2024 / Accepted: 8 April 2024 / Published online: 16 December 2024

Abstract

Neutron-induced gamma-ray imaging is a spectroscopic technique that uses characteristic gamma rays to infer the elemental distribution of an object. Currently, this technique requires the use of large facilities to supply a high neutron flux and a time-consuming detection procedure involving direct collimating measurements. In this study, a new method based on low neutron flux was proposed. A single-pixel gamma-ray detector combined with random pattern gamma-ray masks was used to measure the characteristic gamma rays emitted from the sample. Images of the elemental distribution in the sample, comprising 30×30 pixels, were reconstructed using the maximum-likelihood expectation–maximization algorithm. The results demonstrate that the elemental imaging of the sample can be accurately determined using this method. The proposed approach, which eliminates the need for high neutron flux and scanning measurements, can be used for in-field imaging applications.

Keywords Elemental imaging · Neutron-induced gamma-ray activation · Single-pixel imaging

1 Introduction

The non-destructive testing of objects is essential in applied and fundamental research. Among the various testing parameters, shape is always of prime importance because it is mandatory to observe the surface or interior of a sample before using more advanced characterization technologies, which has attracted interest from both academic researchers and industrial engineers; therefore, many techniques based on imaging and tomography have been developed and used for the structural reconstruction of objects [1, 2]. However, the development of more advanced methods to provide not only the morphology but also the elemental content distribution is worthwhile. Some non-destructive methods, such as laser-induced breakdown spectroscopy (LIBS) and X-ray fluorescence (XRF), have been applied to determine the elemental imaging of samples [3, 4]. However, these methods have limited penetration depth; thus, they are only used for surface or subsurface analyses.

Neutrons are charge-free particles that can easily penetrate materials. This feature renders them particularly suitable for investigating bulk objects; thus, they are ideal probes for non-destructive determination of the physical

This work was supported by the National Natural Science Foundation of China (Nos. 12105143 and 11975121), the China Postdoctoral Science Foundation (No. 2023M741453), the Engineering Research Center of Nuclear Technology Application (No. HJSJYB2020-1), the Key Laboratory of Ionizing Radiation Metering and Safety Evaluation for Jiangsu Province Market Regulation, and the Jiangsu Province Excellent Postdoctoral Program (No. JB23057).

✉ Wen-Bao Jia
jiawenbao@163.com

✉ Da-Qian Hei
heidq@lzu.edu.cn

[1] Department of Ionizing Radiation and Medical Engineering, Jiangsu Institute of Metrology, Nanjing 210023, China

[2] Institute of Nuclear Analytical Technology, Nanjing University of Aeronautics and Astronautics, Nanjing 211106, China

[3] China Nuclear Power Engineering Co., Ltd, Beijing 100840, China

[4] School of Nuclear Science and Technology, Lanzhou University, Lanzhou 730000, China

structure and elemental composition of bulk samples. Neutron imaging has been developed as a reliable non-destructive testing technique in the form of neutron radiography and tomography. As many nuclides have sharp neutron absorption peaks in the epithermal neutron energy region, the composition of the sample can be obtained by analyzing the neutron spectra. Thus, in combination with neutron spectral measurements, this technique, also called neutron energy resonance imaging (NERI), can be used to determine the elemental distribution of a sample [5]. This technique primarily relies on a pulsed neutron source. The neutron spectrum can be determined using a time-of-flight (TOF) spectrometer, which is the standard equipment for measuring the energies of neutrons of a pulse source. Some leading spallation neutron sources, such as ORNL (USA), ISIS (UK), PSI (Switzerland), and CSNS (China), have built these platforms and have been applied in nuclear material detection, archaeometry, and material science [6–9]. Relatively small accelerators such as laser-driven proton accelerators have also been proposed for NERI [10].

Neutron-induced gamma-ray activation is a technology based on thermal neutron capture (TNC) and inelastic neutron scattering (INS) reactions [11, 12]. The nuclides react with neutrons and emit prompt gamma rays, which are then identified and quantified by analyzing the energies and intensities of gamma rays; these have been widely applied for elemental composition analysis. For example, this technology has been applied in environmental science (water, soil, sediment, etc.) [13, 14], threat material detection [15], and determination of industrial materials such as coal, cement, and well logging [16–18]. It has also been demonstrated in imaging applications as diverse as the visualization of drugs for cancer treatment, detection of nuclear materials, elemental imaging for in vivo measurements, and archaeometry [19–21]. Compared with the NERI technique, neutron-induced gamma-ray imaging can be performed using a neutron source with a continuous model and greater sensitivity for light elements.

Most studies were performed by scanning a sample with a collimated neutron beam and/or using a collimated single detector to collect gamma rays [22]. Elemental imaging information was obtained by moving the sample. Consequently, the detection equipment must be installed in reactors or spallation sources capable of supplying a high neutron flux ($10^7 - 10^9 \mathrm{cm}^{-2} \cdot \mathrm{s}^{-1}$) to obtain sufficient signal counts. The spatial resolution is of the order of a few millimeters, and the acquisition of a complete image is also highly time-consuming under these conditions. The measurement time is typically several days, depending on the required number of pixels. Some array gamma-ray detectors, such as the Compton camera, have also been applied for imaging reconstruction [23]. However, because of the coincidence measurements and small size of the pixel crystal, the detection efficiency was unsatisfactory.

These are the main limiting factors, particularly in in-field applications. The gamma-ray signal may be too weak to discriminate when performing elemental imaging with radioactive neutron sources or portable neutron generators. In our previous work, a setup based on a D–T neutron generator was built and used for the elemental distribution analysis of metal materials [24]. However, owing to the low signal-to-noise ratio (SNR), only 4 cm × 4 cm spatial resolution could be achieved. To increase the SNR, one method is the utilization of associated particle (AP) technology, which is mainly used for the D–D and D–T neutron generator. The ^{2}H(d,n)^{3}He and ^{3}H(d,n)^{4}He reactions yield neutrons as well as a ^{3}He ion and a ^{4}He ion, respectively, and the ^{3}He and ^{4}He ions can be considered as APs of the corresponding neutrons. As per conservation of momentum, neutrons and APs are emitted from one another at 180°. Thus, if the direction of the AP is obtained, the path of the neutron can be determined; this is also known as AP collimation. By spatially resolving the APs and setting a time gate after each signal, the neutrons are tagged and their induced gamma rays from the target volume of the sample can be discriminated against the gamma rays produced from the outside volume or other background. This approach has been verified and applied to medical applications [25]. However, the cost of AP neutron generator is high. The detection efficiency is also very low because of the coincidence measurement. Consequently, the detection process is time-consuming, and the spatial resolution of the imaging is unsatisfactory.

A possible solution for the in-field application of neutron-induced gamma-ray imaging is the development of coded aperture imaging [26]. This technology relies on a patterned mask placed in front of a source (light, X-ray, neutrons, etc.) or detector array. The pattern is carefully designed to allow the reconstruction of the object. When an object is imaged through a coded aperture, the acquired image is a superposition of the signals through various regions of the mask. The aperture coding pattern modifies the signal distribution in a known manner. By analyzing the recorded signal intensity, the original object can be effectively reconstructed using decoding algorithms. Numerous patterns such as random arrays, uniform redundant arrays (URA), and modified uniform redundant arrays (MURA) combined with detector arrays have been used for nuclear detection imaging [27–29]. However, as mentioned previously, the efficiency of the detector array is unsatisfactory, particularly for spectrum analysis.

One innovative approach is the utilization of a single-pixel detector combined with various coded masks, known as single-pixel imaging. In this approach, a large size detector is used, which can effectively record the gamma-ray spectrum. It operates in a manner similar to coded aperture

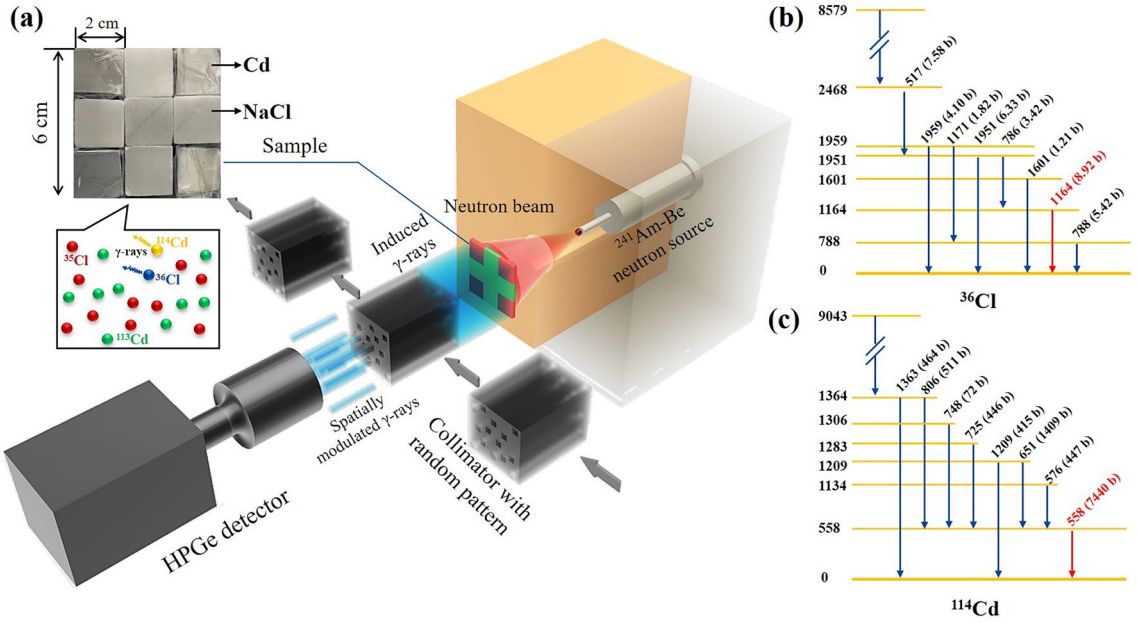

Fig. 1 (Color online) **a** Schematic diagram of the neutron-induced gamma-ray imaging setup. **b**, **c** Decay scheme of ^{36}Cl and ^{114}Cd for partial gamma rays, respectively

imaging. However, single-pixel imaging modulates the signal over time instead of space. In contrast to the highly pixelated position-sensitive detectors used in coded aperture imaging, the modulated signal is detected by a limited number of time-sensitive detectors; it involves the use of a moving mask to attenuate incoming particles. This approach shows promise for enabling efficient and effective imaging with simplified hardware and reduced costs and has been successfully used in many imaging technologies, including those based on terahertz waves, X-rays, visible light, and neutrons [30–32].

In this study, the feasibility of a single-pixel imaging technique for neutron-induced gamma-ray imaging was verified. The gamma rays emitted from the sample to the single-pixel detector were spatially modulated by inserting a series of coded collimators. By analyzing the signals in the presence of each collimator, two-dimensional (2D) images of different elements can be reconstructed, which requires a much lower flux intensity and number of measurements than traditional methods.

2 Materials and methods

2.1 Experimental setup

Figure 1(a) illustrates the experimental setup. An ^{241}Am–Be radioactive neutron source with an activity of 0.3 Ci was placed at the center of a paraffin box, and neutrons were led through a channel with a diameter of 10 cm. As shown in the inset in Fig. 1(a), an object containing Cd and NaCl was placed along the path of the neutron beam. Four 1-mm-thick Cd plates were positioned at the four corners whereas five 5-mm-thick NaCl plates were placed in the remaining regions. When the target nuclides (^{113}Cd and ^{35}Cl) captured thermal neutrons through ^{35}Cl (n, γ) ^{36}Cl and ^{113}Cd (n, γ) ^{114}Cd reactions and entered the excited state, various gamma rays were produced from their de-excitation. The inset shows an image of the sample and illustration of thermal neutron capture reactions. Figure 1(b) and (c) shows the partial decay schemes of ^{36}Cl and ^{114}Cd, respectively, with high thermal neutron-capture cross-sections. The gamma rays used for image reconstruction were 558 keV (Cd) and 1164 keV (Cl) because of their large cross-sections. Various collimators with random patterns of blocked pixels were placed behind each sample. The characteristic gamma rays were spatially modulated after passing through the collimator mask and collected using a hyperpure germanium (HPGe) detector.

2.2 Single-pixel imaging method

In neutron-induced gamma-ray imaging, the net peak area of prompt gamma rays emitted from a sample can be calculated using the following equation [11]:

$$A = \frac{m}{M}\Phi N_{\mathrm{A}}\sigma\varepsilon t, \tag{1}$$

where A is the net peak area, m (g) and M (g · mol^{-1}) are the mass and molar mass of the nuclide, respectively, Φ (cm^{-2}· s^{-1}) is the average thermal neutron flux within the sample, N_A is Avogadro's number, σ (cm^2) is the partial thermal neutron capture cross-section, ε is the detection efficiency, and t (s) is the measurement time.

The basis of this technique is to use various masks and detect the signals of correlations between the masks and the sample. An image can be reconstructed by multiplying each mask by the corresponding signal. For an image with the total number of pixels $N = P_1 \times P_2$, Eq. (1) can be expressed as

$$A = \sum_{n=1}^{N} \Phi_n \varepsilon_n m_n \frac{N_A \sigma}{M} t, \tag{2}$$

where m_n is the mass of the nuclide in the nth pixel, Φ_n is the thermal neutron flux in nth pixel, and ε_n is the detection efficiency for nth pixel. For each pixel, it becomes an isotropic volume gamma-ray source with pixel dimensions after thermal neutron irradiation. These gamma rays move through and interact with samples. Because of these interactions, some gamma rays lose energy and disappear, whereas others exit the sample and traverse the collimator to the HPGe detector, where they are counted. In this study, the ratio of the counted gamma rays to the number of gamma rays emitted from the pixel volume source is defined as the pixel detection efficiency.

Inspection of Eq. (2) reveals that the parameters M, N_A, Φ_n, σ , and t are constants for a specific sample and the given measurement conditions. The measured net peak area depends on m_n and ε_n. If the aim is to use only L ($L < N$) measurements for image reconstruction, the principle of the proposed method can be summarized as follows:

$$A = [\varepsilon_n][m_n], \tag{3}$$

where $[A]$ is a $L \times 1$ column vector, $[m_n]$ is the image with N pixels ordered in a $N \times 1$ vector, $[\varepsilon_n]$ is a $L \times N$ detection efficiency matrix, whose lth ($1 \le l \le L$) row corresponds to the lth measurements. The number of pixels in an image depends on the efficiency matrix.

In this study, the maximum-likelihood expectation–maximization (MLEM) algorithm is used to reconstruct the image. The MLEM algorithm, which is valid for data with a Poisson distribution, has been widely used for image reconstruction in computed tomography (CT), positron emission tomography (PET), and single-photon emission computed tomography (SPECT) [33–35]. The gamma rays induced by neutrons are Poisson distributed, and compared with traditional numerical algorithms, MLEM can achieve high-resolution image reconstruction through iterative calculations, especially for cases with low SNR.

The MLEM algorithm is used to calculate the most likely distribution $[m]$ from the measured $[A]$ by assuming

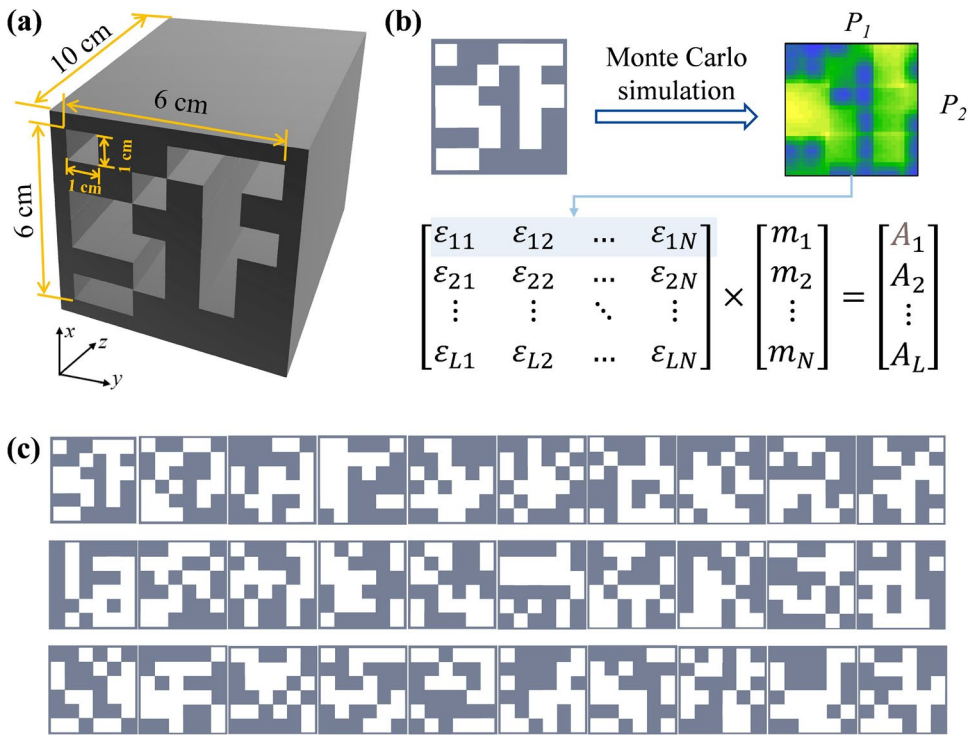

Fig. 2 (Color online) **a** Schematic diagram of one of 30 collimators. **b** Monte Carlo simulations used to calculate the detection efficiency matrix $[\varepsilon_n]$. **c** Patterns of 30 collimators

that the values A_i of $[A]$ are Poisson distributions. This algorithm is expressed as follows [36]:

$$m_n^{k+1} = \frac{m_n^k}{\sum_l \varepsilon_{ln}} \sum_i \varepsilon_{ln} \frac{A_i}{\sum_n \varepsilon_{ln} m_n^k}, \tag{4}$$

where m_n^k and m_n^{k+1} are the reconstructed values for the pixel n after k and $k+1$ iterations, respectively. ε_{ln} is the detection efficiency of pixel n in l_{th} measurement.

2.3 Coded collimator

For neutron-induced gamma-ray imaging technology based on a small-yield neutron source, an object can be considered as a gamma-ray source with low activity after irradiation. To obtain a satisfactory imaging performance, the ratio of the open squares was set to 50%. The random coding method was used to design the collimator patterns. A set of 30 collimators made of iron was used in this study. The schematic of a typical collimator pattern is shown in Fig. 2(a). The iron pixels shield the gamma rays, whereas the opening pixels are transparent to gamma rays. The collimator dimensions were 6 cm × 6 cm × 10 cm ($X \times Y \times Z$). For each pattern, half of the area was blocked and the size of each square opening was set to 1 cm × 1 cm.

In order to solve Eq. (4), the prior detection efficiency matrix $[\varepsilon_n]$ is obtained. The efficiency of a certain energy depends on the HPGe detector performance and the measurement conditions, including the distance between the sample and detector, the geometry, and the materials of the sample. For a small sample, the efficiency curve can be experimentally calibrated using reference gamma ray sources. When the sample is large and cannot be viewed as a point source, the gamma ray self-absorption effect must be corrected. In this study, a Monte Carlo simulation was performed to obtain the efficiency matrix because it is difficult to determine the value experimentally. An image containing 30 × 30 pixels was reconstructed from 30 measurement values to obtain an image with pixel dimensions of 2 mm × 2 mm. The efficiency matrix is presented in Fig. 2(b). Each row of $[\varepsilon_n]$ is associated with a collimator pattern. When the Cd and Cl in each pixel capture thermal neutrons, they can be considered gamma ray sources with energies of 578 and 1164 keV, respectively. Thus, for each pixel, a volume gamma-ray source with isotropic and monoenergy pixel dimensions was defined and placed at the corresponding position. The energy deposition in the HPGe detector was calculated to obtain its detection efficiency. The patterns of the 30 collimators are shown in Fig. 2(c). The efficiency was associated with the collimator pattern, as the iron pixels shielded the gamma rays whereas the opening pixels were transparent to gamma rays.

3 Monte Carlo simulation and experimental

3.1 Benchmark of neutron source

The thermal neutron flux at the sample position was evaluated using an In foil activation method. Foils covered with Al and Cd were irradiated at the sample position. After cooling, the foil was measured using a $LaBr_3$ detector in the lead chamber. The reaction rate R can be expressed as follows [37]:

$$R = \frac{AM\lambda}{N_{\text{A}} mfp\varepsilon(1-e^{-\lambda t_1})e^{-\lambda t_2}(1-e^{-\lambda t_3})}, \tag{5}$$

where A is the net count of delay γ ray peak, M (g·mol^{-1}) is the atomic mass of isotope, λ (s^{-1}) is the decay constant, N_{A} is Avogadro's number, m (g) is the mass of the foil, f is the isotopic abundance, p is the emission probability, ε is the detection efficiency, t_1, t_2 , and t_3 (s) are the irradiation time, cooling time, and measurement time, respectively. Then, the thermal neutron flux ϕ_{th} and epithermal neutron flux ϕ_{epi} can be obtained as follows [37]:

$$\phi_{\text{th}} = \frac{1}{G_{\text{th}} g \sigma_{\text{In}}} [R_{\text{Al}} - R_{\text{Cd}}(1 + \frac{g\sigma}{G_{\text{res}} I} f_1 + \frac{\sigma w'}{G_{\text{res}} I})] \quad , \tag{6}$$

$$\phi_{\text{epi}} = \frac{R_{\text{Cd}}}{I} \quad , \tag{7}$$

where G_{th} and G_{res} are the thermal and epithermal self-shielding factors, respectively. σ_{In} is the thermal neutron reaction cross-section. In the thermal energy range, the cross-section varies inversely with the neutron speed $(1/v)$. g is the correction factor that accounts for departures from the

Table 1 Measurement conditions and parameters of In foil activation

Parameters	In + Cd	In + Al
σ_{In} (barn)	166.41	166.41
G_{th}	0.742	0.742
G_{res}	0.128	0.128
g	1.0194	1.0194
I (barn)	2680.28	2680.28
f_1	0.468	0.468
w'	0.2953	0.2953
λ (s^{-1})	0.000213	0.000213
f	0.957	0.957
ε	0.1016	0.1016
p	0.848	0.848
m (g)	3.75	3.63
A	1236	5956
t_1 (s)	43200	43200
t_2 (s)	120	780
t_3 (s)	600	600

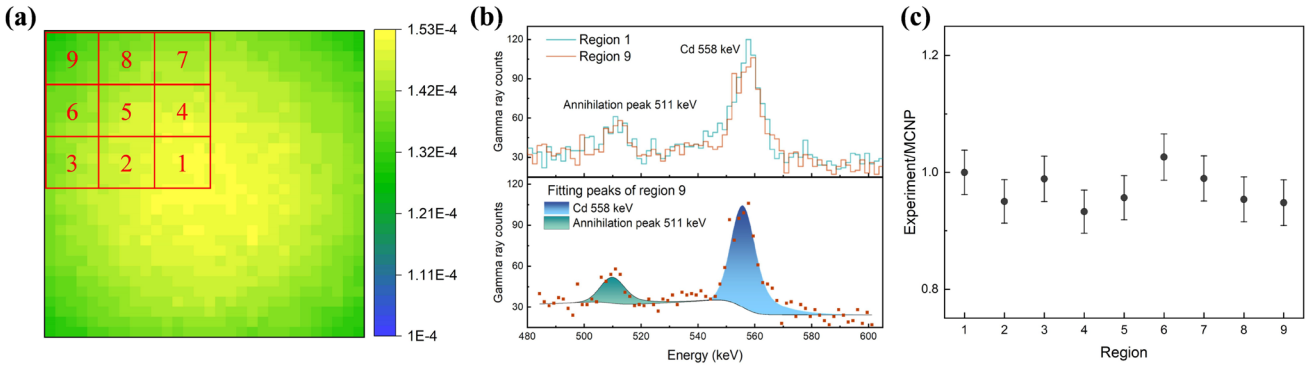

Fig. 3 (Color online) **a** Mapping of thermal neutron flux. **b** Typical gamma ray spectra and fitting peaks. **c** Ratio of Experiment/MCNP for each region

ideal $1/v$ cross-section. I is the resonance integral cross-section, g is the correction factor caused by the neutron energy deviation of $1/v$, which is related to the neutron temperature, f_1 is the correction caused by the energy from 5 kT (the lowest energy of epithermal neutrons is usually taken to be equal to 5 kT) to the epithermal neutrons, w' is the correction caused by the energy from 5 kT to E_{Cd}. The detailed values are listed in Table 1.

A delayed gamma ray 1293 keV of ^{116m}In was used to calculate the thermal neutron flux. The measurement conditions of two foils and some parameters are listed in Table 1. The thermal and epithermal neutron fluxes are $40.2 \pm 1.3\,\mathrm{cm^{-2}s^{-1}}$ and $0.52 \pm 0.01\,\mathrm{cm^{-2}s^{-1}}$, respectively. The uncertainties are mainly derived from the counting statistics of the gamma rays. Compared with large facilities, the thermal neutron flux is very low. The MCNP5 software combined with the ENDF/B-VI cross-section library was used to calculate the thermal neutron flux. The MCNP model of the neutron source was developed in our previous study [38]. The neutron yield of the ^{241}Am − Be source was also evaluated. The thermal neutron flux (< 0.5 eV) in the In foil (ϕ_{MCNP}) was calculated by using F4 tally, and the value was $8.29 \times 10^{-4}\,\mathrm{cm^2}$. Then, the neutron yield can be calculated using ϕ_{th}/ϕ_{MCNP}. The result was $4.82 \times 10^5\,\mathrm{s^{-1}}$. In addition, the thermal neutron flux distribution was evaluated. The neutron ($E_{th} < 0.5$ eV) distribution at the sample position was calculated. A mesh tally with pixels 2 mm × 2 mm was mapped to calculate the distribution. The results are presented in Fig. 3(a).

Benchmark experiments were conducted to verify the simulation results. Owing to the complicated process and low efficiency of foil activation, an alternative method based on a Cd–Zn–Te detector was used to determine the thermal neutron distribution at the sample position. Because the induced gamma rays are produced inside the crystal, the thermal neutron detection efficiency is relatively high [39]. A Cd–Zn–Te detector with dimensions of 1 cm × 1 cm × 0.5 cm (DT-01C1, Imdetek) was used to characterize the thermal neutron distribution. Considering symmetry, the measurements were conducted in only one-quarter of the region. As shown in Fig. 3(a), the measurement regions were divided by 3 × 3 parts (red box) based on the size of the detector.

The acquisition time of the Cd–Zn–Te detector was set to 600 s for each measurement. Typical gamma-ray spectra and fitting peaks are shown in Fig. 3(b). The 558 keV peak was used for comparison with the simulated data. Net peak counts were obtained by subtracting the background signals. For the simulated data, the pixel values of each region were averaged and normalized to the highest experimental value. The results are presented in Fig. 3(c). We observed that the discrepancies were within 10%. A satisfactory agreement between the experimental and simulated data was observed, which indicates the workability of the MCNP simulation.

3.2 Model of HPGe detector

In this study, an N-type HPGe detector (ORTEC: TRANSSPEC) with a relative efficiency of 55% and a resolution of 1.9 keV at 1333 keV was used to detect prompt gamma rays. The signals were collected using a multichannel analyzer and the MAESTRO software [40]. The structural parameters supplied by the detector manufacturer indicated that the diameter and length of the Ge crystal were 67 and 71 mm, respectively. There was an internal hole whose diameter and length are 15 and 60 mm, respectively. The thicknesses of dead layer of the internal hole and the external crystal surfaces are 700 and 0.3 μm, respectively. The Ge crystal was positioned inside an aluminum case with a diameter of 83 mm and length of 106.5 mm. As the parameters of the aluminum case were not provided by the manufacturer, an X-ray radiography system was used to observe the internal position of the crystal and the dimensions of the case. Figure 4(a) shows an image of the HPGe detector.

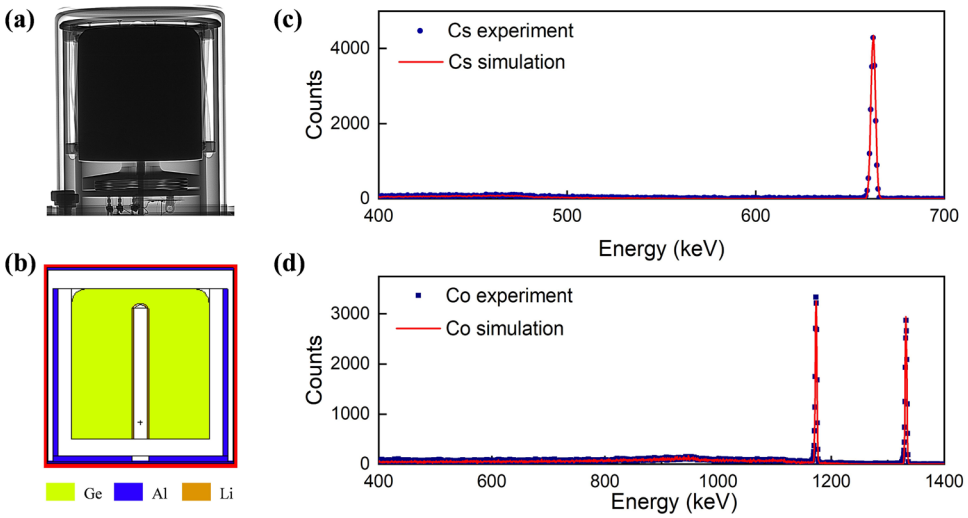

Fig. 4 (Color online) **a** X-ray radiography of HPGe detector. **b** MCNP model. **c**, **d** Simulated and experimental gamma ray spectra of ^{137}Cs and ^{60}Co

An MCNP model of the HPGe detector head was constructed based on these parameters, as shown in Fig. 4(b). The simulated gamma-ray spectrum was calculated using the pulse height tally (F8) and Gaussian energy broadening (GEB) cards. To verify the feasibility of the developed detector model, benchmark measurements were performed with reference to the ^{137}Cs and ^{60}Co point sources. The activities of the ^{137}Cs and ^{60}Co sources at the time of measurement were 9.19×10^4 and 1.20×10^4 Bq, respectively. The emission probabilities of 662 keV (^{137}Cs), 1173 keV, and 1332 keV (^{60}Co) are 0.851, 0.9985, and 0.9998, respectively. The distance between the source and detector surfaces was 15 cm. The acquisition time was 900 s for the live-time model.

The experimental and simulation results are presented in Fig. 4(c) and (d). The simulation results agreed well with the experimental data. The full energy peak efficiencies (FEPEs) of the three peaks were compared. The discrepancies between the experimentally determined and simulated FEPEs were 3.76%, 3.71% and −2.18%, respectively. The main reasons are probably counting statistics and scattering by surrounding materials. The developed model was validated based on these uncertainties.

3.3 Sample measurement and image analyses

To ensure a satisfactory counting statistic, the measurement time was set to 3 h with a live time due to the low thermal neutron flux. The induced gamma-ray spectra of were also recorded using the MAESTRO software. The analysis of the prompt gamma ray peaks was carried out using the GAMMAFIT software [41] because the interference and overlapping of the peaks caused a challenge for accurate peak fitting owing to the poor SNR. In addition, a traditional method with a single collimated detector was also performed; the measurement time was the same, and the square opening was also 1 cm × 1 cm. After setting the measurement time, the neutron damage to the HPGe detector was evaluated by calculating the accumulated neutron fluence. An F4 tally was used to calculate the neutron flux in the HPGe crystal. The average value was approximately 4.71×10^{-5}cm^{-2} and was multiplied by the neutron yield and measurement time. The result was 7.36×10^6cm^{-2}, which is acceptable compared to published work [42, 43].

The image quality was evaluated using the structural similarity index measure (SSIM) and root mean square error (RMSE) [44]. SSIM is a widely used metric that reflects the visual similarity between a true image and a reconstructed image; an SSIM value close to unity indicates that the two images are similar. The SSIM is defined as follows:

$$\mathrm{SSIM} = \frac{(2\mu_r\mu_t + C_1)(2\sigma_{r,t} + C_2)}{(\mu_r^2 + \mu_t^2 + C_2)(\sigma_r^2 + \sigma_t^2 + C_2)}, \tag{8}$$

where μ_r, μ_t, σ_r , and σ_t are the average and standard deviations of the reconstructed and true images, respectively; $\sigma_{r,t}$ is the covariance between the reconstructed and true images; C_1 and C_2 are constants set to avoid zero denominators. In this study, C_1 and C_2 were set to 0.1.

RMSE reflects the difference in pixel values between a true image and a reconstructed image. A smaller value indicates that the reconstructed image has a smaller statistical deviation. The RMSE is defined as follows:

$$\mathrm{RMSE} = \sqrt{\frac{1}{N}\sum_{i=1}^{N}(P_i^r - P_i^t)^2}, \tag{9}$$

where N is the pixel number, P_i^r and P_i^t are the ith pixel values of the reconstructed and true images, respectively.

Furthermore, the spatial resolution of the proposed system was calculated using the edge spread function (ESF), which describes the spreading or blurring of edges or sharp

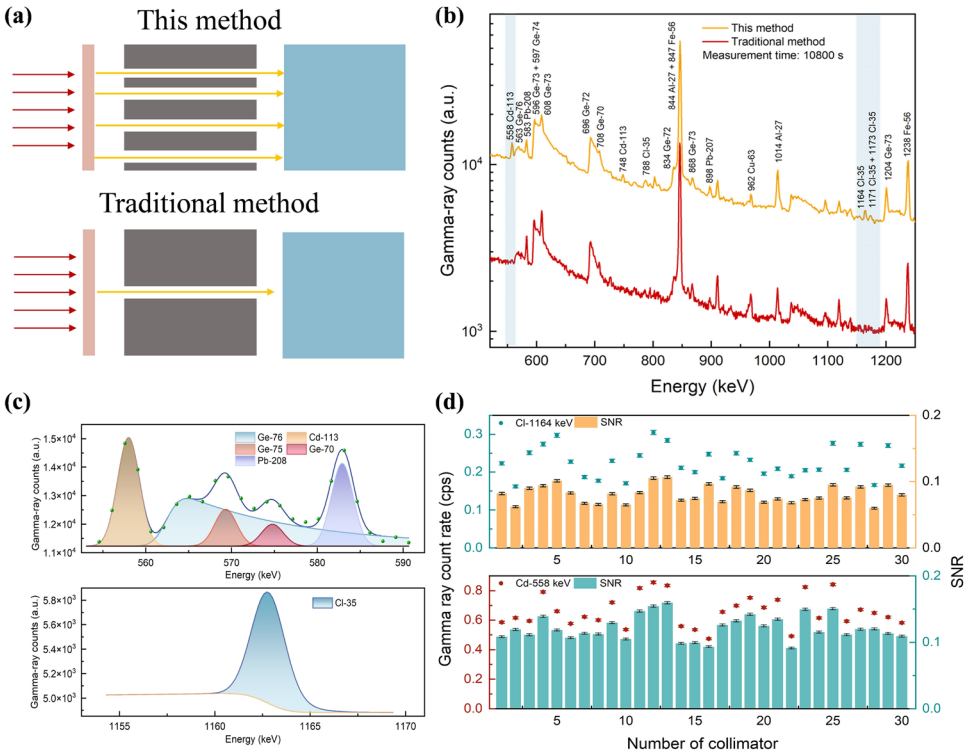

Fig. 5 (Color online) **a** Schematic diagram of two methods **b** Gamma-ray spectra in the energy range 520–1250 keV acquired during 10800 s for this method (Orange) and the traditional method (Red). **c** Fitting of Cd peak and Cl peak. **d** Count rates and SNRs of Cl peak and Cd peak for each collimator

transitions in an image [45]. This quantifies how the intensity values change across an edge, providing information on the quality of image sharpness. The ESF is obtained by analyzing the pixel values along a line perpendicular to an edge or transition in an image. The line is usually taken across the transition from background to foreground or vice versa. By analyzing the intensity values along this line, the ESF represents the changes in intensity from one side of the edge to the other.

4 Results and discussion

4.1 Analysis of induced gamma-ray spectra

The enlarged gamma-ray spectra of the region of interest for the pattern collimator and the traditional method are shown in Fig. 5(a) and (b). The spectra essentially consist of induced gamma rays of elements from the sample and other materials, including the collimator, shielding, and detector materials. The major isotopes and their gamma-ray energies are marked. The most prominent peaks were produced by iron and aluminum through the inelastic scattering reactions ^{56}Fe (n,n$'\gamma$) ^{56}Fe and ^{27}Al (n,n$'\gamma$) ^{27}Al. These gamma rays originated mainly from the collimator and detector housing materials, which correspond to the 847 keV and 1238 keV of the Fe peaks, as well as 844 keV and 1014 keV of the Al peaks. For the 962 keV of the Cu peak, they were mainly emitted from the detector cold finger. Moreover, Pb peaks could be observed because they were components of the shielding material. Another fraction of induced gamma rays was emitted from the detector crystal, the neutrons reacted with the germanium nucleus which led to the 608 keV, 868 keV, and 1204 keV peaks through INC reaction, as well as the formation of the so-called germanium triangles 597 keV, 696 keV, and 834 keV through INS reaction.

The overall count rates in the interesting region were 8160 cps for the proposed method and 1800 cps for the traditional method. This is because more square openings lead to more background gamma rays and neutrons interacting with HPGe detector. Although the background signal was approximately four times higher than that of the traditional method, the peaks of Cd and Cl were still readily observed. The 558 keV and 748 keV Cd peaks were identified. However, the 651 keV Cd peak could not be observed because it was affected by the 597 keV germanium triangle. For the gamma rays emitted from Cl, the 788 keV, 1164 keV, 1171 keV, and 1173 keV peaks were identified. All of these peaks could not be observed in the spectra acquired using the traditional method. As mentioned above, the intensities of the 558 keV Cd and 1164 keV Cl peaks were analyzed using the GAMMAFIT software. An example is shown in Fig. 5(c). The count rates and corresponding SNRs for the two peaks in the 30 measurements are shown in Fig. 5(d). Under the

present measurement conditions, the average SNRs were approximately 8% for the 1164 keV Cl peak and 12% for the 558 keV Cd peak.

4.2 Correction of neutron field

For neutron-induced gamma-ray imaging, the neutron field inside a sample should ideally be maintained. However, as shown in Fig. 3(a), the thermal neutron flux decreases at the edge owing to the isotropic emission of ^{241}Am–Be neutron source. Moreover, the neutron beam is attenuated, particularly for elements with high TNC macroscopic cross-sections, which leads to a neutron self-shielding effect. To solve this problem, neutron radiography/tomography can be used to experimentally determine the neutron field. However, neutron imaging using a low-yield source is not feasible. An alternative approach is to calculate the neutron flux inside each pixel using Monte Carlo simulation [46]. Correction of the solid angle and neutron self-shielding effect can be performed as follows:

$$P_i^{\mathrm{C}} = P_i^{\mathrm{r}} \frac{\phi_{i,\mathrm{d}}}{\phi_{i,\mathrm{r}}} \frac{\phi_{\mathrm{f,max}}}{\phi_{i,\mathrm{f}}} \tag{10}$$

where $P_i^{\mathrm{C}}$and P_i^{r} are the i_{th} pixel values of the corrected and reconstructed images, respectively, and $\phi_{i,\mathrm{f}}$ and $\phi_{\mathrm{f,max}}$ are the ith pixel and maximum thermal neutron flux as shown in Fig. 3(a). $\phi_{i,\mathrm{r}}$ is the thermal neutron flux inside the ith pixel, $\phi_{i,\mathrm{d}}$ is the one for "diluted sample," where the density of sample is reduced by a factor of 1000. Neutron beam attenuation is negligible and reflects neutron self-shielding [47]. These values are obtained using a mesh tally.

4.3 Image reconstruction

After obtaining the net peak areas of the 30 measurements, the Cd and Cl images were reconstructed using the MLEM

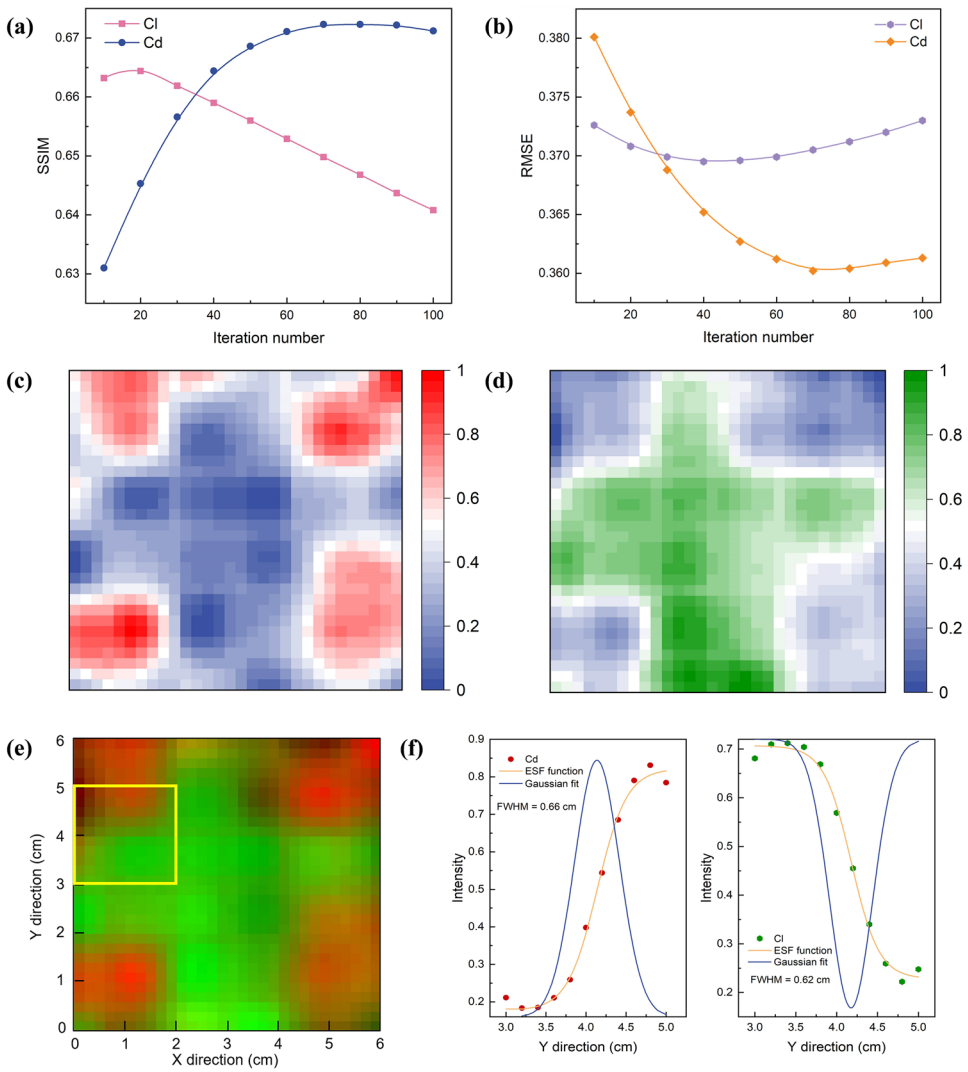

Fig. 6 (Color online) **a** SSIM as a function of the iteration number. **b** RMSE as a function of the iteration number. **c**, **d** Reconstructed element imaging of the sample. The reconstructions on the left and right are the Cd and Cl images, respectively. **e** RGB map of the sample, where red represents Cd and green represents Cl. **f** ESFs of Cd and Cl images

algorithm. The SSIM and RMSE for different numbers of iterations were calculated, as shown in Fig. 6(a) and (b). For SSIM, the optimal number of iterations was 20 (Cl images) and 70 (Cd images). For RMSE, the optimal number of iterations was 40 (Cl image) and 70 (Cd images). This was primarily because the effect of noise on the reconstructed image tended to increase with the number of iterations when the SNR was small. Finally, the number of iterations is set to 70. The corresponding reconstructed images are presented in Fig. 6(c) and (d). The color bar indicates the normalized content, ranging from 0 (minimum value) to 1 (maximum value). The SSIM values of the Cd and Cl images are 0.67 and 0.65, respectively, whereas the RMSE of the Cd and Cl images is 0.36 and 0.37, respectively. For easier visualization, as shown in Fig. 6(e) shows the red–green–blue (RGB) map of the elemental distributions. The reconstructed images show the elemental distribution of the sample accurately. The results show that the distributions of Cd (red) and Cl (green) can be clearly distinguished. The regions occupied by Cd are observed in the four corners, whereas the remaining regions correspond to Cl.

Figure 6(f) shows the ESFs and corresponding fitting functions of two element images. The ESF function is obtained by averaging the pixel values within the yellow box in Fig. 6(e), horizontally followed by fitting with a sigmoid curve (orange line). Subsequently, the first derivative of the sigmoid curve is calculated and fitted using a Gaussian function (blue line). The full width at half maximum (FWHM) of the Gaussian curve is defined as the spatial resolution. The results show that the spatial resolutions of Cd and Cl images are 0.66 cm and 0.62 cm, respectively. The results reported by Laszlo [48] and Kluge [49], obtained using a collimated neutron beam at the BNC and FRM II reactors, were approximately 0.2–0.3 cm. The result reported by Chen Mayer [23] using a Compton camera detector on the NIST reactor was approximately 0.3 cm. Compared with these studies, we achieved a similar level of resolution using a low-flux neutron source.

In this study, the element images were reconstructed using a relatively low flux, resulting in data with a low SNR and a long measurement time. In practical applications, the measurement time can be reduced by using a neutron source with a higher neutron yield. Scintillator detectors (NaI, BGO, $LaBr_3$, etc.) combined with a full gamma ray spectrum analytical algorithm can also be used in certain specific cases owing to their high detection efficiencies and counting statistics. In addition, the collimator masks can be optimized to improve the quality of the reconstructed element images when working at a low SNR or low sampling rates. A rotating collimator can be used because the modulation varies with the rotation angle. The incident gamma rays produce a fluctuating signal corresponding to the modulation at different angles [32].

When applying this technique to real objects with unknown information, it must be combined with other techniques for a comprehensive analysis. The acquisition of accurate geometrical information and chemical compositions is vital when constructing a Monte Carlo model. Optical scanning and X-ray tomography are effective techniques for obtaining accurate geometrical information [50]. An initial scan measurement can be conducted over a relatively large volume to provide a rough estimate of chemical composition. Based on the data, a preliminary Monte Carlo model was developed. Subsequently, its parameters were adjusted to accurately simulate the detection efficiency matrix and neutron field. This fine-tuning process involves iterations in which the compositions assigned to individual pixels are continuously refined. Through this iterative refinement, a state of self-consistency was achieved, thereby generating an elemental map with a high spatial resolution [47].

5 Conclusion

In this paper, we reported an experimental implementation of elemental imaging using neutron-induced gamma rays combined with a single-pixel detector. Rather than relying on scanning measurements or array detectors, the proposed approach used collimator masks with random patterns for imaging. This approach verifies the feasibility of neutron-induced gamma-ray imaging using portable neutron sources and has the potential to broaden the applicability of imaging techniques across the fields of biology, medical diagnosis, materials science, and engineering.

Author Contributions All authors contributed to the study conception and design. Material preparation, data collection, and analysis were performed by CC, Y-JX, X-RX, J-YG, DZ, Y-ZC, A-YS, X-WL, W-BJ, and D-QH. The first draft of the manuscript was written by CC and all authors commented on previous versions of the manuscript. All authors read and approved the final manuscript.

Data availability The data that support the findings of this study are openly available in Science Data Bank at https://cstr.cn/31253.11.sciencedb.10795 and https://www.doi.org/10.57760/sciencedb.10795.

Declarations

Conflict of interest The authors declare that they have no conflict of interest.

References

1. R.F. Ziesche, T. Arlt, D.P. Finegan et al., 4D imaging of lithium-batteries using correlative neutron and X-ray tomography with a virtual unrolling technique. Nat. Commun. **11**, 777 (2020). https://doi.org/10.1038/s41467-019-13943-3

2. Y.L. Chen, H.K. Wang, S.Y. Zhang et al., Hi'ct: a pixel sensor-based device for ion tomography. Nucl. Sci. Tech. **34**, 111 (2023). https://doi.org/10.1007/s41365-023-01251-x
3. W. Xu, Z. Du, S. Liu et al., Perspectives of XRF and XANES applications in cryospheric sciences using Chinese SR facilities. Condens. Matter **3**, 29 (2018). https://doi.org/10.3390/condmat3040029
4. C. Fabre, D. Devismes, S. Moncayo et al., Elemental imaging by laser-induced breakdown spectroscopy for the geological characterization of minerals. J. Anal. Atom. Spectrom. **33**, 1345–1353 (2018). https://doi.org/10.1039/c8ja00048d
5. T. Shinohara, T. Kai, K. Oikawa et al., The energy-resolved neutron imaging system, RADEN. Rev. Sci. Instrum. **91** (2020). https://doi.org/10.1063/1.5136034
6. A. Tremsin, J. Vallerga, Unique capabilities and applications of Microchannel Plate (MCP) detectors with medipix/timepix readout. Radiat. Meas. **130**, 106228 (2020). https://doi.org/10.1016/j.radmeas.2019.106228
7. E.P. Cippo, A. Borella, G. Gorini et al., Imaging of cultural heritage objects using neutron resonances. J. Anal. Atom. Spectrom. **26**, 992–999 (2011). https://doi.org/10.1039/c0ja00256a
8. J. Yang, J. Zhou, L. Zhang et al., Recent measurements at the CSNS towards the construction of a nMCP detector for the energy resolved neutron imaging instrument. Nucl. Instrum. Methods A **1003**, 165322 (2021). https://doi.org/10.1016/j.nima.2021.165322
9. E.R.C. Ruiz, N. Stalder, J. Lee, et al., Prospects of spectroscopic neutron imaging: optimizing experimental setups in battery electrolyte research. Phys. Chem. Chem. Phys. 24993–25007 (2023). https://doi.org/10.1039/D3CP03434H
10. M. Zimmer, S. Scheuren, A. Kleinschmidt et al., Demonstration of non-destructive and isotope-sensitive material analysis using a short-pulsed laser-driven epi-thermal neutron source. Nat. Commun. **13**, 1173 (2022). https://doi.org/10.1038/s41467-022-28756-0
11. Z. Révay, Determining elemental composition using prompt γ activation analysis. Anal. Chem. **81**, 6851–6859 (2009). https://doi.org/10.1021/ac9011705
12. T. Randriamalala, M. Rossbach, E. Mauerhofer et al., Fangas: a new instrument for (n, n' γ) reaction measurements at FRM II. Nucl. Instrum. Methods A **806**, 370–377 (2016). https://doi.org/10.1016/j.nima.2015.10.026
13. Y. Zhang, Z. Yao, B. Tang et al., In situ experimental measurement of mercury by combining PGNAA and characteristic X-ray fluorescence. Appl. Radiat. Isot. **168**, 109488 (2021). https://doi.org/10.1016/j.apradiso.2020.109488
14. A. Kavetskiy, G. Yakubova, N. Sargsyan et al., Scanning mode application of neutron–gamma analysis for soil carbon mapping. Pedosphere **29**, 334–343 (2019). https://doi.org/10.1016/S1002-0160(19)60806-4
15. D. Sudac, M. Pavlovic, J. Obhodas et al., Detection of Chemical Warfare (CW) agents and the other hazardous substances by using fast 14 MeV neutrons. Nucl. Instrum. Methods A **971**, 164066 (2020). https://doi.org/10.1016/j.nima.2020.164066
16. X. Zhong, L. Chen, B. Wang et al., A spectrometer with baseline correction and fast pulse pile-up rejection for prompt gamma neutron activation analysis technology. Rev. Sci. Instrum. **89**, 123504 (2018). https://doi.org/10.1063/1.5049517
17. S. Sharma, L. Vo, M.P. Pfeifer et al., Bulk material interrogation experimental results and validation with Geant4 for replacement of dangerous radiological sources in oil-well logging industries. Appl. Radiat. Isot. **170**, 109602 (2021). https://doi.org/10.1016/j.apradiso.2021.109602
18. Z. Li, H. Xiao, Y. Huawei et al., Lithology affects and correction of neutron porosity logging using D–D source. Nucl. Tech. **45**, 050501 (2022). https://doi.org/10.11889/j.0253-3219.2022.hjs.45.050501. (**in Chinese**)
19. L. Szentmiklósi, Z. Kis, Characterizing nuclear materials hidden in lead containers by neutron-tomography-driven prompt gamma activation imaging (PGAI-NT). Anal. Methods **7**, 3157–3163 (2015). https://doi.org/10.1039/c5ay00199d
20. N. Koshikawa, A. Omata, M. Masubuchi et al., Activation imaging of drugs with hybrid Compton camera: a proof-of-concept study. Appl. Phys. Lett. **121**, 193701 (2022). https://doi.org/10.1063/5.0116570
21. Q. Dai, Q. Yang, X. Bao et al., The development of boron analysis and imaging in boron neutron capture therapy (BNCT). Mol. Pharm. **19**, 363–377 (2022). https://doi.org/10.1021/acs.molpharmaceut.1c00810
22. Z. Kis, L. Szentmiklósi, T. Belgya, NIPS-NORMA station-A combined facility for neutron-based nondestructive element analysis and imaging at the budapest neutron centre. Nucl. Instrum. Methods A **779**, 116–123 (2015). https://doi.org/10.1016/j.nima.2015.01.047
23. H.H. Chen-Mayer, S. Brown, H. Yang, Feasibility study of Compton imaging for PGAA. J. Radioanal. Nucl. Chem. **322**, 1729–1738 (2019). https://doi.org/10.1007/s10967-019-06818-w
24. D. Hei, W. Jia, C. Cheng et al., Feasibility study of fast neutron-induced gamma ray imaging of large sample based on DT neutron generator. Nucl. Instrum. Methods B **492**, 7–14 (2021). https://doi.org/10.1016/j.nimb.2021.01.014
25. M.R. Abel, D.S. Koltick, L.H. Nie, Associated particle neutron elemental imaging in vivo: a feasibility study. Med. Phys. **43**, 5964–5972 (2016). https://doi.org/10.1118/1.4964791
26. M.J. Cieślak, K.A. Gamage, R. Glover, Coded-aperture imaging systems: past, present and future development—a review. Radiat. Meas. **92**, 59–71 (2016). https://doi.org/10.1016/j.radmeas.2016.08.002
27. S. Sun, Y. Liu, X. Ouyang, Design and performance evaluation of a coded aperture imaging system for real-time prompt gamma-ray monitoring during proton therapy. Radiat. Phys. Chem. **174**, 108891 (2020). https://doi.org/10.1016/j.radphyschem.2020.108891
28. X. Li, Z. Zhang, D. Li et al., Comparison of the modified uniformly redundant array with the singer array for near-field coded aperture imaging of multiple sources. Nucl. Instrum. Methods A **1051**, 168230 (2023). https://doi.org/10.1016/j.nima.2023.168230
29. Z. Zhou, S.G. Li, Q.S. Tan et al., Optimization method of Hadamard coding plate in γ-ray computational ghost imaging. Nucl. Sci. Tech. **34**, 13 (2023). https://doi.org/10.1007/s41365-022-01164-1
30. Y.H. He, Y.Y. Huang, Z.R. Zeng et al., Single-pixel imaging with neutrons. Sci. Bull. **66**, 133–138 (2021). https://doi.org/10.1016/j.scib.2020.09.030
31. R.I. Stantchev, X. Yu, T. Blu et al., Real-time terahertz imaging with a single-pixel detector. Nat. Commun. **11**, 2535 (2020). https://doi.org/10.1038/s41467-020-16370-x
32. E. Hahamovich, S. Monin, Y. Hazan et al., Single pixel imaging at megahertz switching rates via cyclic Hadamard masks. Nat. Commun. **12**, 4516 (2021). https://doi.org/10.1038/s41467-021-24850-x
33. Y. Zhu, A.K. Jha, D.F. Wong et al., Image reconstruction in fluorescence molecular tomography with sparsity-initialized maximum-likelihood expectation maximization. Biomed. Opt. Express **9**, 3106–3121 (2018). https://doi.org/10.1364/BOE.9.003106
34. J. Cui, K. Gong, N. Guo et al., PET image denoising using unsupervised deep learning. Eur. J. Nucl. Med. Mol. Imaging **I**(46), 2780–2789 (2019). https://doi.org/10.1007/s00259-019-04468-4
35. H. Yang, B. Dong, W. Gu et al., Transmission reconstruction algorithm by combining maximum-likelihood expectation maximization and a convolutional neural network for radioactive drum

characterization. Appl. Radiat. Isot. **184**, 110172 (2022). https://doi.org/10.1016/j.apradiso.2022.110172
36. H.F. Xiao, Q.X. Zhang, H.Y. Tan et al., The study of a neutron spectrum unfolding method based on particle swarm optimization combined with maximum likelihood expectation maximization. Nucl. Sci. Tech. **34**, 60 (2023). https://doi.org/10.1007/s41365-023-01200-8
37. C. Cheng, Z. Wei, D. Hei et al., MCNP benchmark of a ^{252}Cf source-based PGNAA system for bulk sample analysis. Appl. Radiat. Isot. **158**, 109045 (2020). https://doi.org/10.1016/j.apradiso.2020.109045
38. Z. Dong, L. Xuwen, Z. Ronghua et al., Design and calibration of a depth-of-interaction detector for neutrons and gamma rays. Nucl. Tech. (in Chinese) **46**, 070402 (2023)
39. X. Liang, D. Zhao, W. Jia et al., Characterization of thermal neutron distribution of an Am–Be neutron source setup by CdZnTe detector. Appl. Radiat. Isot. **196**, 110778 (2023). https://doi.org/10.1016/j.apradiso.2023.110778
40. ORTEC, MAESTRO multichannel analyzer emulation software. MAESTRO-32 v7 User's Manual. https://www.ortec-online.com/productscn/application-software/maestro-mca
41. L. Szentmiklósi, Fitting special peak shapes of prompt gamma spectra. J. Radioanal. Nucl. Chem. **315**, 663–670 (2018). https://doi.org/10.1007/s10967-017-5589-z
42. Z. Jian-Yong, F. Cheng-Dong, M. Xiao-Hu et al., Effects due to a Pu-C source on a HPGe detector and the corresponding neutron shielding. Chin. Phys. C **35**, 660 (2011). https://doi.org/10.1088/1674-1137/35/7/011
43. E. Seabury, C.D. Van Siclen, J. McCabe et al., Neutron damage in mechanically-cooled high-purity germanium detectors for field-portable Prompt Gamma Neutron Activation analysis (PGNAA) systems. (IEEE Xplore, 2013), pp. 1–4, https://doi.org/10.1109/NSSMIC.2013.6829527
44. S. Sato, J. Kataoka, J. Kotoku et al., First application of the super-resolution imaging technique using a Compton camera. Nucl. Instrum. Methods A **969**, 164034 (2020). https://doi.org/10.1016/j.nima.2020.164034
45. S. Sun, X. Ouyang, A feasibility study on the application of separable coded masks to X-ray fluorescence imaging. J. Anal. Atom. Spectrom. **36**, 210–223 (2021). https://doi.org/10.1039/d0ja00413h
46. W.B. Jia, Y.Z. Chen, D.Q. Hei et al., Prompt gamma-ray activation imaging based on multi coded-aperture collimators. Nucl. Tech. 45, 100201 (2022). https://doi.org/10.11889/j.0253-3219.2022.hjs.45.100201. **(in Chinese)**
47. L. Szentmiklósi, Z. Kis, B. Maróti et al., Correction for neutron self-shielding and gamma-ray self-absorption in prompt-gamma activation analysis for large and irregularly shaped samples. J. Anal. Atom. Spectrom. **36**, 103–110 (2021). https://doi.org/10.1039/d0ja00364f
48. Z. Kis, T. Belgya, L. Szentmiklósi, Monte Carlo simulations towards semi-quantitative prompt gamma activation imaging. Nucl. Instrum. Methods A **638**, 143–146 (2011). https://doi.org/10.1016/j.nima.2011.02.062
49. E. Kluge, C. Stieghorst, Z. Révay et al., Optimization and characterization of the PGAI-NT instrument's Neutron Tomography setup at MLZ. Nucl. Instrum. Methods A **932**, 1–15 (2019). https://doi.org/10.1016/j.nima.2019.04.011
50. B. Maroti, B. Polonkai, V. Szilagyi et al., Joint application of structured-light optical scanning, neutron tomography and position-sensitive prompt gamma activation analysis for the non-destructive structural and compositional characterization of fossil echinoids. NDT & E Int. **115**, 102295 (2020). https://doi.org/10.1016/j.ndteint.2020.102295